

# UCLA

## UCLA Previously Published Works

### Title

A Numerical Investigation of Turbulent Flow and Heat Transfer in Rectangular Channels With Elliptic Scale-Roughened Walls

### Permalink

<https://escholarship.org/uc/item/2s02r8dm>

### Journal

Journal of Heat Transfer, 135(8)

### ISSN

0022-1481

### Authors

Zhou, Feng  
Catton, Ivan

### Publication Date

2013-06-27

### DOI

10.1115/1.4024278

Peer reviewed

# A Numerical Investigation of Turbulent Flow and Heat Transfer in Rectangular Channels With Elliptic Scale-Roughened Walls

Feng Zhou

e-mail: zhoufeng@ucla.edu

Ivan Catton

e-mail: catton@ucla.edu

Department of Mechanical and Aerospace Engineering, University of California, 48-121 Engineering IV, 420 Westwood Plaza, Los Angeles, CA 90095

*In the present paper, rectangular channels with six types of elliptic scale-roughened walls for heat transfer enhancement are numerically studied. Heat transfer and fluid flow characteristics for sixteen different scale-roughened models (with the scale height varying in the range from 1 mm to 2.5 mm) are numerically predicted using commercial computational fluid dynamics (CFD) code, ANSYS CFX. The turbulent model employed is the  $k-\omega$  based shear-stress transport (SST) model with automatic wall function treatment. In the performance evaluation, we use a “universal” porous media length scale based on volume averaging theory (VAT) to define the Reynolds number, Nusselt number, and friction factor. It is found that heat transfer performance is most favorable when the elliptic scales are oriented with their long axis perpendicular to the flow direction, while the scales elongated in the flow direction have lower Nusselt numbers and pressure drops compared with the circular scale-roughened channels. Results indicate that the scale-shaped roughness strongly spins the flow in the spanwise direction, which disrupts the near-wall boundary layers continuously and enhances the bulk flow mixing. With the flow marching in a more intense spiral pattern, a 40% improvement of heat transfer enhancement over the circular scale-roughened channels is observed. [DOI: 10.1115/1.4024278]*

*Keywords:* rectangular channel, elliptic scale, surface roughness, heat transfer enhancement, volume averaging theory, VAT, CFD, turbulence, SST

## 1 Introduction

Heat transfer enhancement plays a more and more important role in areas, such as electronics cooling, compact heat exchangers, power plants, gas turbine airfoil cooling, etc. A variety of techniques [1] for heat transfer enhancement have been developed, including ribs [2–6], pin fins [7–9], dimpled surfaces [10–12], surfaces with arrays of protrusions [13], and surface roughness. All of these devices not only act to increase secondary flows and turbulence levels to enhance bulk flow mixing and to form coherent fluid motions in the form of streamwise oriented vortices but also provide some heat transfer augmentation by increasing surface areas for convective heat transfer [1]. The design objective of these techniques is to significantly enhance convective heat transfer without substantially increasing in the streamwise pressure drop penalty.

In order to cope with the ever-mounting cooling duty of heat transfer devices, a new heat transfer enhancement surface geometry was developed by Chang et al. [14–18] using deepened circular scale roughness. The surface scales are arranged in a staggered manner in-line on opposing walls. The authors compared  $\overline{Nu}/Nu_\infty$  and  $\overline{f}/f_\infty$  of the scale-roughened surface with the flow and heat transfer results reported by different research groups for rib-roughened channels [2–6] and dimpled surfaces [10]. The heat transfer enhancement of the scale-roughened surface was surprisingly good compared with rib-roughened and dimpled surfaces and the channel with forward flow performs better than that with backward flow. A previous numerical study presented by the

authors [19] also showed that the scale-roughened surfaces have the potential to improve the convective heat transfer in heat sinks for electronics cooling.

In the spirit of thermal engineering, one might ask “should the scale shape proposed by Chang et al. [14] necessarily be the optimum? Will the heat transfer be enhanced or decreased if the scales are elongated or squeezed? How will the scale depth affect the performance of the scale-roughened channels? What is the mechanism of heat transfer enhancement by scales?” To answer these questions, a numerical investigation as well as a qualitative study incorporating CFD flow visualization was conducted by the authors.

Six new types of elliptic scale-roughened surfaces, which include elliptic scales with the long axis aligned parallel to the flow direction ( $P_2/P_1=0.3, 0.5, 0.7$ ) and elliptic scales with the long axis aligned perpendicularly to the flow direction ( $P_2/P_1=1.43, 2, 3.33$ ) are proposed and numerically simulated to compare with the original circular scale-roughened surface. The scale arrangement and the print shapes of the seven types of scales, including the circular scale are shown in Figs. 1 and 2, respectively. To get a more vivid picture of the different scales, 3D models and dimensions of them are tabulated in Table 1. The elliptic scale cases 2, 3, 4, and 5, and the circular scale cases, with four different scale depths are also simulated to show the effects of the scale depth. The objective of this work is to determine whether or not the elliptic scales can further enhance the heat transfer performance, to show how the scale depth and orientation play a role and to unveil the mystery of heat transfer augmentation by scales, which should be helpful to the readers who are interested in heat transfer enhancement techniques. This is the first time that a surface with elliptic scale roughness is proposed. No similar research could be found in the open literature.

Contributed by the Heat Transfer Division of ASME for publication in the JOURNAL OF HEAT TRANSFER. Manuscript received July 1, 2012; final manuscript received April 16, 2013; published online June 27, 2013. Assoc. Editor: James A. Liburdy.

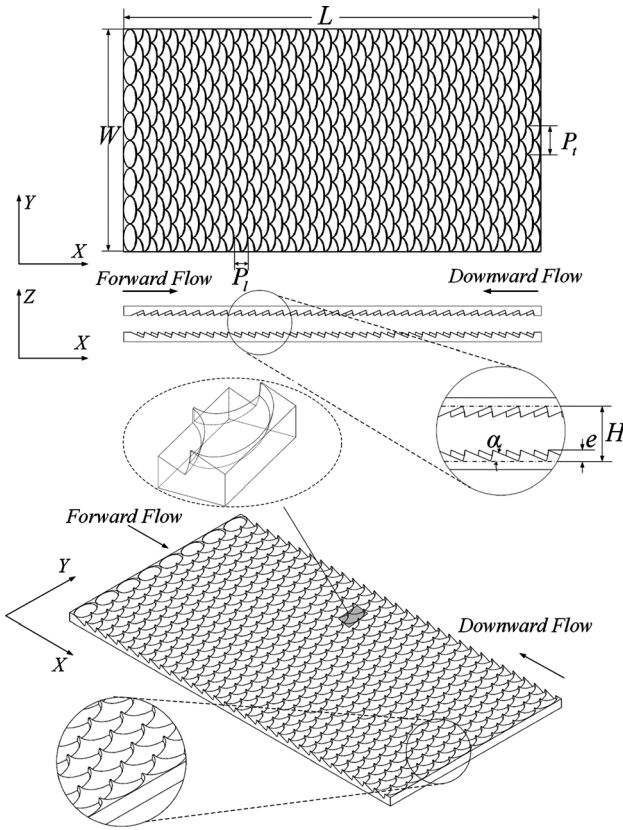


Fig. 1 Geometrical details of one of the elliptic scale-roughened surfaces

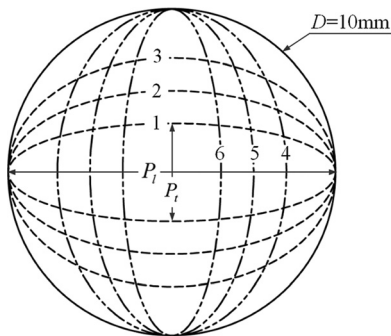


Fig. 2 Print shapes of the elliptic scales

## 2 Numerical Method and Procedures

### 2.1 Computational Domain and Boundary Conditions.

Given a rectangular channel with periodic surface augmentation in the spanwise direction, a passage with width of one scale in the spanwise direction and the whole channel length in the flow direction was developed for the computational domain, see Fig. 3. Because of the thickness of the channel walls, the air velocity profile at the entrance of the channel is not uniform. The computational domain is then extended upstream 0.5 times the streamwise channel length, so that a uniform velocity profile could be applied at the inlet. The downstream boundary of the computational domain is located at the distance of a channel length from the trailing edge of the wall in the streamwise direction. The boundary conditions applied to the computational domain are tabulated in Table 2.

**2.2 Grid System.** The grid systems for all the scale-roughened channel models were built by ANSYS meshing tool. Due

to the roughness of the wall, an unstructured tetramesh is created for the scale-roughened test channel, with prism layers being inserted in the near-wall region. In the extended regions, a coarser and structured hex-mesh is adopted to conserve computational resources. A grid system with a gradual variation in and after the scale-roughened test channel is used to avoid the undesirable effect of an abrupt grid width change in the computing region, see Fig. 4.

Grid independence tests were carefully addressed by recursive refinement and comparison between the numerical simulation results. Take the circular scale case as an example, where grid systems with 697,849, 1,728,574, 2,639,059, 3,860,677, and 6,985,479 elements were tested, and comparing the local variables (temperature and velocity) and the average Nusselt number and friction factor of the finest grid with the second finest one, a 0.5% difference was yielded. To save computer resources and also get a reasonable accuracy, the fourth grid system was adopted and the numerical predictions can be regarded as grid-independent. With the turbulence predictions employed, the meshes near the fluid solid interface are fine enough to resolve the boundary layer behavior close to the no-slip wall. For all the simulation cases,  $y^+$  values in the near-wall region are less than 1.

**2.3 Mathematical Model.** The air flow is assumed to be three-dimensional, steady state, and turbulent. Since the maximum Mach number for all the cases studied is less than 0.06, the flow is considered to be incompressible. Buoyancy and radiation heat transfer effects are not taken into consideration. The three-dimensional governing equations for continuity, momentum, and energy are as follows:

(1) Continuity equation

$$\frac{\partial \rho u_i}{\partial x_i} = 0 \quad (1)$$

(2) Momentum equation

$$\rho u_j \frac{\partial u_i}{\partial x_j} = \frac{\partial}{\partial x_j} \left[ (\mu + \mu_t) \frac{\partial u_i}{\partial x_j} \right] - \frac{\partial p}{\partial x_i} \quad (2)$$

(3) Energy equation

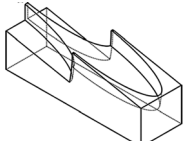
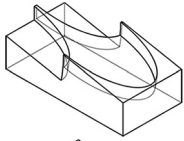
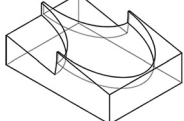
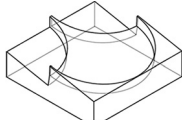



$$\rho u_j \frac{\partial T}{\partial x_j} = \frac{\partial}{\partial x_j} \left[ \left( \frac{\mu}{Pr} + \frac{\mu_t}{Pr_t} \right) \frac{\partial T}{\partial x_j} \right] \quad (3)$$

The  $k-\omega$  based SST model with automatic wall function treatment is used to predict the turbulent flow and heat transfer through the channel. The SST model blends the robust and accurate formulation of the  $k-\omega$  model in the near-wall region with the free-stream independence of the  $k-\epsilon$  model in the far field. The SST model gives a highly accurate prediction of the onset and the amount of flow separation under adverse pressure gradients by the inclusion of transport effects into the formulation of the eddy viscosity. This results in a major improvement in terms of flow separation predictions. Bardina et al. [20] showed that comparing with other eddy viscosity models, the SST model captures separation under an adverse pressure gradient well, therefore the near-wall turbulence could be accurately predicted, which plays an important role in the accurate prediction of the turbulent heat transfer.

Menter [21,22] proposed the equations for the SST model as

$$\frac{D(\rho k)}{Dt} = \tilde{P}_k - \beta^* \rho k \omega + \frac{\partial}{\partial x_j} \left[ (\mu + \sigma_k \mu_t) \frac{\partial k}{\partial x_j} \right] \quad (4)$$

**Table 1 The different scale shapes for the present numerical studied**

Tested cases	3D models \ flowdirection	$P_t$ , mm	$P_1$ , mm	$P_t/P_1$	$e$ , mm	$\alpha$ , deg	$H$ , mm
Elliptic scale 1		3	10	0.3	2	11.54	10
Elliptic scale 2		5	10	0.5	1, 1.5, 2, 2.5	5.74, 8.63, 11.54, 14.48	10
Elliptic scale 3		7	10	0.7	2	11.54	10
Circular scale		10	10	1	1, 1.5, 2, 2.5	5.74, 8.63, 11.54, 14.48	10
Elliptic scale 4		10	7	1.43	2	16.60	10
Elliptic scale 5		10	5	2	1, 1.5, 2, 2.5	11.54, 17.46, 23.58, 30	10
Elliptic scale 6		10	3	3.33	2	41.81	10

$$\frac{D(\rho\omega)}{Dt} = \alpha\rho S^2 - \beta\rho\omega^2 + \frac{\partial}{\partial x_i} \left[ (\mu + \sigma_\omega\mu_t) \frac{\partial\omega}{\partial x_i} \right] + 2(1 - F_1)\rho\sigma_{\omega_2} \frac{1}{\omega} \frac{\partial k}{\partial x_i} \frac{\partial\omega}{\partial x_i} \quad (5)$$

in which

$$CD_{k\omega} = \max \left( 2\rho\sigma_{\omega_2} \frac{1}{\omega} \frac{\partial k}{\partial x_j} \frac{\partial\omega}{\partial x_j}, 10^{-10} \right) \quad (7)$$

where the blending function  $F_1$  is defined by

$$F_1 = \tanh \left\{ \left[ \min \left[ \max \left( \frac{\sqrt{k}}{\beta^* \omega y}, \frac{500\nu}{y^2\omega} \right), \frac{4\rho\sigma_{\omega_2} k}{CD_{k\omega} y^2} \right] \right]^4 \right\} \quad (6)$$

The turbulent eddy viscosity is computed from

$$\nu_t = \frac{a_1 k}{\max(a_1\omega, SF_2)} \quad a_1 = 0.31 \quad (8)$$

where  $S$  is the invariant measure of the strain rate and  $F_2$  is a second blending function defined by

$$F_2 = \tanh \left\{ \left[ \max \left( 2 \frac{\sqrt{k}}{\beta^* \omega y}, \frac{500\nu}{y^2\omega} \right) \right]^2 \right\} \quad (9)$$

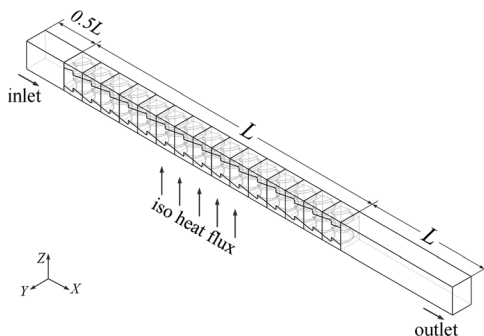


**Fig. 3 Computational domain. The length of the extended region was not drawn in scale.**

**Table 2 Boundary conditions**

Inlet	$u = \text{const}, v = w = 0, T = \text{const}$
Outlet	$\frac{\partial u_i}{\partial x} = \frac{\partial T}{\partial x} = 0$
Eight surfaces of the extended region	Symmetric, slip, and adiabatic wall
Interface between air and solid	No-slip, no thermal resistance
The bottom of the scale-roughened wall	Iso heat flux
The other surfaces	Symmetric

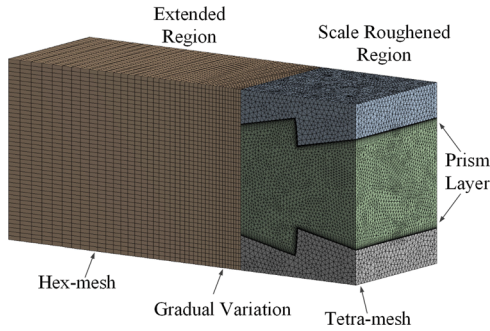


**Fig. 4 Example of the grid system. Only part of the whole model is shown.**

To prevent the build-up of turbulence in stagnation regions, a production limiter is used in the SST model

$$P_k = \mu_t \frac{\partial u_i}{\partial x_j} \left( \frac{\partial u_i}{\partial x_j} + \frac{\partial u_j}{\partial x_i} \right) \rightarrow \tilde{P}_k = \min(P_k, 10 \cdot \beta^* \rho k \omega) \quad (10)$$

Each of the constants is a blend of the corresponding constants of the  $k$ - $\epsilon$  and the  $k$ - $\omega$  model

$$\varphi = F_1 \varphi_1 + (1 - F_1) \varphi_2 \quad (11)$$

The constants for this model take the following values [22]

$$\begin{aligned} \beta^* &= 0.09, \\ \alpha_1 &= 5/9, \beta_1 = 3/40, \sigma_{k1} = 0.85, \sigma_{\omega1} = 0.5, \\ \alpha_2 &= 0.44, \beta_2 = 0.0828, \sigma_{k2} = 1, \sigma_{\omega2} = 0.856 \end{aligned} \quad (12)$$

The CFX solver solves the discrete system of linearized equations using a multigrid accelerated incomplete lower upper factorization technique and rapidly removes local errors in the solution. The algebraic multigrid scheme is used to accelerate the convergence of the solver by computing the corrections on a series of coarse grid levels. The CFD code solves the Reynolds-averaged Navier–Stokes equations with a high resolution scheme for the advection terms as well as turbulence numerics. The fully coupled momentum and energy equations are solved simultaneously. In all simulations, the second-order upwind scheme is used for the discretization of the momentum and energy equations. The RMS type residual for solution convergence criteria is set to be  $10^{-5}$  for the momentum balance and  $10^{-6}$  for the energy equation [9,23].

### 3 Parameter Definition and Data Reduction

To validate the CFD simulation results, the Reynolds number, hydraulic diameter, Nusselt number, and friction factor are defined the same as that used by Chang et al. [14] However, in the following performance evaluation, we use a “universal” porous media length scale suggested by by Travkin and Catton [24]

$$D_h = \frac{4\langle m \rangle}{S_w} \quad (13)$$

which was also recognized by Whitaker [25] when he used a very similar (differing by a constant) length scale to correlate heat transfer for a wide variety of morphologies. Zhou et al. [26] also showed that using the “porous media” length scale is very beneficial in collapsing complex data yielding simple heat transfer and friction factor correlations.

To calculate the length scale by Eq. (13), two parameters, porosity  $\langle m \rangle$  and specific surface  $S_w$  need to be defined. For the rectangular channel with elliptic scale-roughened surface, a

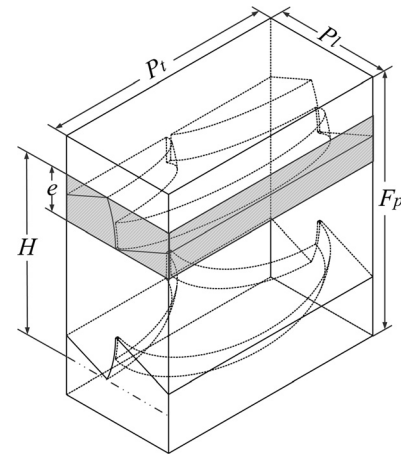


**Fig. 5 REV for a PFHS with scale-roughened surfaces**

representative elementary volume (REV), shown in Fig. 5, which repeats in both the cross-stream and flow directions was chosen. The porosity of the REV is

$$\langle m \rangle = 1 - \frac{\Delta\Omega_s}{\Delta\Omega} = \frac{H - 2\kappa e}{F_p} \quad (14)$$

in which,  $\Delta\Omega$  is the volume of the REV defined as

$$\Delta\Omega = P_t P_l F_p \quad (15)$$

$\Delta\Omega_s$  is the volume of the solid part of the REV defined by

$$\Delta\Omega_s = P_t P_l (F_p - H) + 2\kappa e P_t P_l \quad (16)$$

in which  $\kappa$  is the ratio of the solid volume of the scale to the total volume of the  $e \times P_t \times P_l$  slab. It can easily be shown that  $\kappa$  is a constant and  $\kappa = \frac{3}{4} - \frac{\pi}{8}$ . The specific surface area,  $S_w$ , is defined as wetted surface per unit volume

$$S_w = \frac{A_w}{\Delta\Omega} = \frac{2P_t P_l + \pi \left[ \frac{3}{4}(P_t + P_l) - \frac{1}{2} \sqrt{P_t P_l} \right] e}{P_t P_l F_p} \quad (17)$$

Therefore, for the present scale-roughened channel,  $D_h$  is defined as

$$D_h = \frac{4\langle m \rangle}{S_w} = \frac{4P_t P_l (H - 2\kappa e)}{2P_t P_l + \pi \left[ \frac{3}{4}(P_t + P_l) - \frac{1}{2} \sqrt{P_t P_l} \right] e} \quad (18)$$

The Reynolds number defined using the VAT suggested length scale is

$$\text{Re}_{D_h} = \frac{\rho \bar{u} D_h}{\mu} \quad (19)$$

The averaged Nusselt number is defined as

$$\text{Nu}_{D_h} = \frac{q D_h}{k_f (\bar{T}_s - \bar{T}_f)} \quad (20)$$

The Fanning friction factor for validation is defined as

$$f_{D_h} = \frac{\Delta p}{\frac{1}{2} \rho \bar{u}^2} \frac{D_h}{4L} \quad (21)$$

We still need a third parameter to evaluate the overall effectiveness of the heat transfer devices, which not only takes the conjugate effect into consideration and describe the physical phenomena involved in the cooling processes but also has a wide application, allowing one to compare different geometries with different fluid properties.

The pumping power per unit volume is

$$P_p''' = \frac{P_p}{\Omega} = \frac{\Delta p \dot{m}}{\rho \Omega} = 2f_{D_h} Re_{D_h}^3 \frac{\mu^3 \langle m \rangle}{\rho^2 D_h^4} \quad (22)$$

For constant pumping power per unit volume

$$\left( P_p''' \right)_E = \left( P_p''' \right)_\infty \quad (23)$$

and the relationship between friction and Reynolds number can be expressed as follows:

$$\left( 2f_{D_h} Re_{D_h}^3 \frac{\mu^3 \langle m \rangle}{\rho^2 D_h^4} \right)_E = \left( 2f_{D_h} Re_{D_h}^3 \frac{\mu^3 \langle m \rangle}{\rho^2 D_h^4} \right)_\infty \quad (24)$$

It should be noted that, for smooth channel, Eq. (18) is reduced to  $D_h = 2H$ , which is the same as traditional length scale used for parallel channel. Therefore, in the following presentation, the subscript  $D_h$  will be omitted for reference parameters. From Eq. (24), we get

$$Re_\infty = Re_{D_h} \left( \frac{f_{D_h}}{f_\infty} \right)^{1/3} \left( \frac{\langle m \rangle}{\langle m \rangle_\infty} \right)^{1/3} \left( \frac{D_{h\infty}}{D_h} \right)^{4/3} \frac{\mu}{\mu_\infty} \left( \frac{\rho_\infty}{\rho} \right)^{2/3} \quad (25)$$

The thermal enhancement factor,  $\eta_{\text{eff}}$ , is defined as the ratio of the heat transfer coefficient,  $h$ , of an augmented surface to that of a smooth surface,  $h_\infty$ , at a constant pumping power

$$\begin{aligned} \eta_{\text{eff}} &= \frac{q/\Delta T}{(q/\Delta T)_\infty} \Big|_{P_p} = \frac{h}{h_\infty} \Big|_{P_p} = \frac{Nu_{D_h} D_{h\infty} k}{Nu_\infty D_h k_\infty} \Big|_{P_p} \\ &= \frac{Nu_{D_h} D_{h\infty}}{Nu_\infty D_h} \left( \frac{f_{D_h}}{f_\infty} \right)^{-1/3} \left( \frac{\langle m \rangle}{\langle m \rangle_\infty} \right)^{-1/3} \left( \frac{D_{h\infty}}{D_h} \right)^{-4/3} \\ &\quad \times \left( \frac{k}{k_\infty} \right) \left( \frac{\mu_\infty}{\mu} \right) \left( \frac{\rho_\infty}{\rho} \right)^{-2/3} \end{aligned} \quad (26)$$

Simplify Eq. (26), we get

$$\begin{aligned} \eta_{\text{eff}} &= \frac{Nu_{D_h}}{Nu_\infty} \left( \frac{f_{D_h}}{f_\infty} \right)^{-1/3} \left( \frac{\langle m \rangle}{\langle m \rangle_\infty} \right)^{-1/3} \left( \frac{D_{h\infty}}{D_h} \right)^{-1/3} \\ &\quad \times \left( \frac{k}{k_\infty} \right) \left( \frac{\mu_\infty}{\mu} \right) \left( \frac{\rho_\infty}{\rho} \right)^{-2/3} \end{aligned} \quad (27)$$

The effectiveness factor defined by Eq. (27) gives more information about the characteristics of the heat transfer devices and is not limited to the same fluid when reporting data. The last three terms in Eq. (27) could be eliminated when the fluids for the comparative reference case and the enhanced channels are the same and have equivalent properties. For the present study, Eq. (27) could be further simplified to

$$\eta_{\text{eff}} = \frac{Nu_{D_h}}{Nu_\infty} \left( \frac{f_{D_h}}{f_\infty} \right)^{-1/3} \left( \frac{\langle m \rangle}{\langle m \rangle_\infty} \right)^{-1/3} \left( \frac{D_{h\infty}}{D_h} \right)^{-1/3} \quad (28)$$

in which  $Nu_\infty$  and  $f_\infty$  are Dittus–Boelter correlation and Blasius equation for turbulent flow

$$Nu_\infty = 0.023 Re^{0.8} Pr^{0.4} \quad (29)$$

$$f_\infty = 0.079 Re^{-0.25} \quad (30)$$

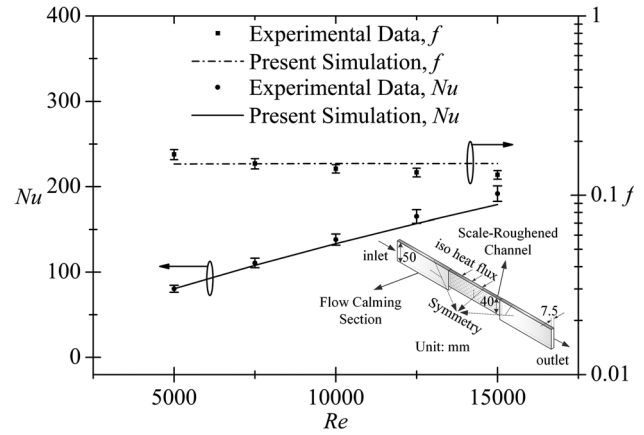


Fig. 6 Validation of the present CFD simulation by comparing with experimental data by Chang et al. [14]

## 4 Results and Discussion

In the following presentation, the rectangular channel with circular scale-roughened surfaces experimentally tested by Chang et al. [14] are numerically simulated to verify and validate the numerical model and CFD code first. After that, flow and heat transfer results for sixteen different models of scale-roughened channels are numerically predicted and comparisons are presented in three parts. The first is a quantitative comparison of heat transfer enhancements and pressure drop penalties to show the effects of Reynolds number, scale pitch ratio, and scale depth. The second is a comprehensive comparison from the viewpoint of overall performance or heat dissipation efficiency. The third is a qualitative comparison to give insight into the flow behavior through different channels.

**4.1 Validation and Verification.** To verify the computational model and the method adopted in numerical simulation, preliminary computations were first conducted for a scale-roughened channel which had the same dimensions as the one experimentally tested by Chang et al. [14]. From Fig. 6, we can see that the maximum deviation of the Nusselt number and the friction factor from experiment is 6.3% and 12.1% with the average deviation being around 3.5% and 5.8%, respectively. Our predicted results and the experimental data agree very well, thereby showing the reliability of the physical model and the adopted numerical method.

**4.2 Effect of Reynolds Number and Scale Pitch Ratio.** The comparisons of flow and heat transfer characteristics of the different scale-roughened channels, in terms of Nusselt number and pressure drop, are plotted in Figs. 7 and 8.

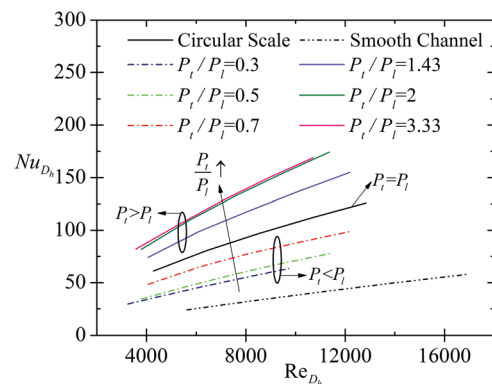


Fig. 7 Nusselt number versus Reynolds number

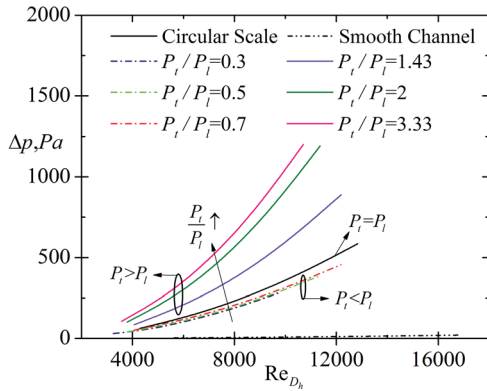


Fig. 8  $\Delta p$  versus Reynolds number

From Fig. 7, it is clear that the elliptic scales with the long axis aligned perpendicularly to the flow direction offer a surprisingly high Nusselt number. The channel with the scale pitch ratio of  $P_t/P_1 = 1.43$  provides more than a 22% increase in the Nusselt number compared with the circular scale-roughened channel, and if further increase the ratio of scale pitches  $P_t/P_1$  to 2, another 17% increment is seen (about 40% over circular scale case in total). It should be noted that since a different length scale is used in the present work, the Nusselt number ratio between the elliptic scale-roughened and smooth channel flows ( $Nu_{D_h}/Nu_{\infty}$ ) is around 3.1. However, if the same length scale was used as Chang et al. [14], the ratio,  $Nu/Nu_{\infty}$ , would be around 6.5 for this case, compared with  $Nu/Nu_{\infty} \approx 4.5$  reported by Chang et al. [14] for circular scale-roughened surface. If we increase the scales to a pitch ratio of 3.33, no significant difference is seen. As to the elliptic scales with the long axis aligned parallel to the flow direction, all the three numerically tested cases with  $P_t/P_1$  from 0.3 to 0.7 showed worse performance than circular scale case. The  $P_t/P_1 = 0.7$  case shows a 21% decrement while a 40% decrease is seen when  $P_t/P_1$  decreases to 0.5. If we further elongate the scales in the flow direction, no sharp deterioration is seen, which is similar to the increasing trend when we squeeze the scales. Based on the above analysis, it seems that the range of scale pitch ratio that has a prominent effect on the heat transfer augmentation is  $0.5 \leq P_t/P_1 \leq 2$ .

Comparisons of pressure drop are presented in Fig. 8. Since heat transfer enhancement is usually accompanied by a high pressure penalty, it is not surprising that the pressure drop increases as the scale pitch ratio,  $P_t/P_1$ , increases. The elliptic scales with  $P_t/P_1 = 2$  and 1.43 have around 70% and 40% higher pressure drop than the circular scales, respectively, at lower Reynolds number. As Reynolds number increases, the percentage of pressure drop increment further increases, comparing with an almost linear

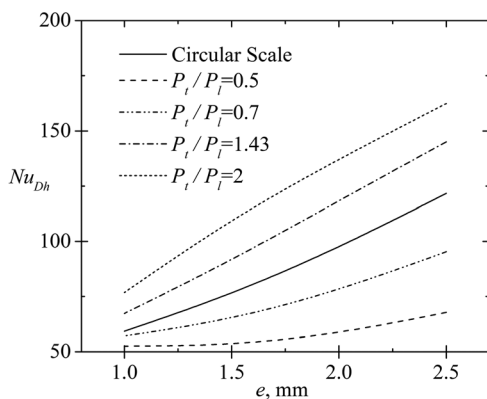


Fig. 9 Nusselt number versus scale height,  $Re_{D_h} = 10,000$

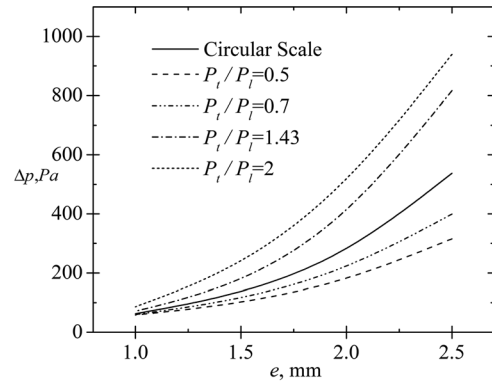


Fig. 10 Pressure drop versus scale height,  $Re_{D_h} = 10,000$

increasing trend of Nusselt number with Reynolds number. Therefore, the overall efficiency of the scale-roughened channel is expected to decrease as the Reynolds number increases. For the elliptic scales with  $P_t/P_1 < 1$ , the pressure drop could be as much as 75% lower than the circular scales, which is not unexpected considering their poorer heat transfer performance. Similar to the Nusselt number, the effect of the scale pitch ratio on pressure drop concentrates mainly in the range  $0.5 \leq P_t/P_1 \leq 2$ . This provides a rough idea for engineers who are interested in using elliptic scale-roughened surfaces for heat transfer enhancement purposes.

**4.3 Effect of Scale Height.** The effects of scale height on the heat transfer enhancement and pressure penalty of scale-roughened surfaces with Reynolds number being at 10,000 are shown in Figs. 9 and 10, taking the circular scale case and elliptic scale cases with  $P_t/P_1 = 0.5, 0.7, 1.43,$  and 2 as an example. As the scale height increases, more solid roughness penetrates into the near-wall flow, forcing the fluid to divert and mix with the bulk channel flow. Therefore, higher Nusselt number and form drag are expected. It should be noted that the depth of the scale cannot be increased unboundedly since it is limited by the longitudinal pitch of the scale which is the theoretical maximum of the depth (with attack angle  $\alpha = \pi/2$ ). Also, for a specific scale longitudinal pitch, a large scale depth means a large scale attack angle which would be more difficult to fabricate. Besides, the scale depth cannot be larger than half the thickness of the fins, supposing one would like to apply this technique to heat transfer devices with fins.

**4.4 Comprehensive Comparison.** Figures 7–10 compare the channels with different scale pitch ratios and scale heights regarding heat transfer enhancement and pressure drop increment separately. However, increasing Nusselt number is accompanied by increasing pressure drop which is undesirable. Thus, based

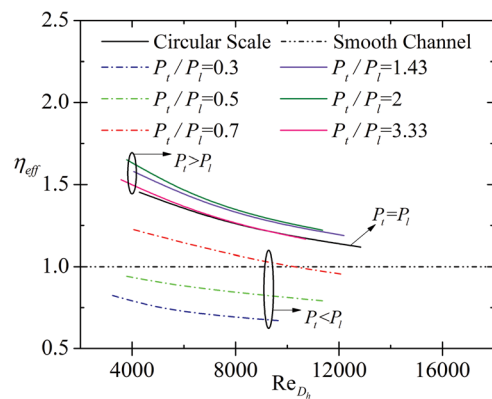
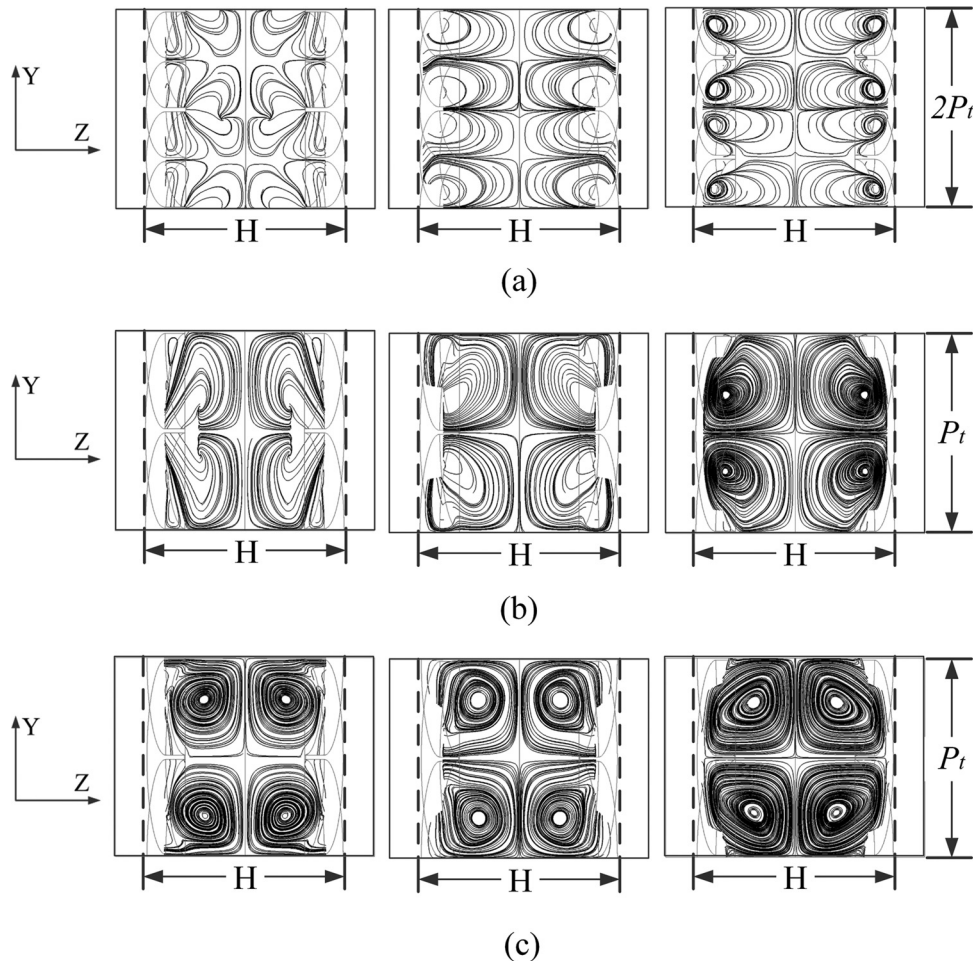


Fig. 11 Effectiveness factor versus Reynolds number



**Fig. 12 Streamlines on the planes normal to flow direction at  $Re = 10,000$ : (a) elliptic scale 2,  $P_t/P_1 = 0.5$ ; (b) circular scale,  $P_t/P_1 = 1$ ; and (c) elliptic scale 5,  $P_t/P_1 = 2$**

only on Figs. 7–10, it is almost impossible to come to a final conclusion as to which type of channels performs better than the others if both the heat transfer enhancement and power consumption are considered simultaneously. Therefore, a comprehensive performance comparison should be made to evaluate the effectiveness of different types of channels, see Fig. 11.

It is found that all the elliptic scale-roughened channels with  $P_t/P_1 > P_1$  as well as circular scale case have higher effectiveness factor than 1 in the present Reynolds number region. Compared with the circular scale-roughened channel, the elliptic scale cases with  $P_t/P_1 = 2$  and  $P_t/P_1 = 1.43$  show 11% and 7% enhancements, respectively. Further increasing the pitch ratio  $P_t/P_1$  to 3.33 decreases the effectiveness factor to almost the same as circular scale case. On the other hand, the elliptic scale cases with  $P_t/P_1 < 1$  have no advantage compared with the circular scale-roughened channel. The two cases with  $P_t/P_1$  smaller than 0.5 even have a  $\eta_{eff}$  lower than 1. Therefore, it is obvious that the elliptic scale-roughened surface with the long axis aligned perpendicularly to the flow direction shows a considerable potential to further enhance the heat transfer performance, while the channels with the long axis aligned parallel to the flow direction do not perform the circular scale-roughened channels.

Another thing that should be noted is that the effectiveness factors of all types of scale-roughened surfaces decrease with increasing Reynolds number, as expected from observations obtained when the Nusselt number and pressure drop were analyzed separately.

**4.5 Mechanism of Heat Transfer Enhancement by Scales.** To have a qualitative view into the flow behavior, Fig. 12 provides insight into the local distributions of the streamlines for

three cross-sections in the  $y$ - $z$  planes normal to the flow direction at  $Re = 10,000$  for three tested channels, which include elliptic scale case 2 ( $P_t/P_1 = 0.5$ ), the circular scale case ( $P_t/P_1 = 1$ ), and the elliptic scale case 5 ( $P_t/P_1 = 2$ ). The three planes divide the scale whose centerline is located at  $x = 100$  mm equally to show how the streamlines develop when the fluid flows through one cycle of the scale-roughened channel. From Fig. 12(a) for elliptic scale case 2 with  $P_t/P_1 = 0.5$ , it is found that when the flow starts entering the channel, some cone-shaped streamlines are formed above the scales. After that the flow starts spinning in the spanwise direction. However, the spinning is not as strong as that for circular scales and squeezed scales. Similar to the elongated scale case, the streamlines for the circular scale case, see Fig. 12(b), have a cone shape at the leading edge of the scale and then strong flow spinning is seen. Different from the above two cases, no cone-shaped streamlines are seen for the squeezed scale-roughened channel, see Fig. 12(c). Instead, more intense rotation is found all the way from the leading edge to the trailing edge of the scale. The strong spinning of the flow breaks the near-wall boundary layers continuously and enhances the bulk flow mixing. It is easy for the readers to turn the plane streamlines into 3D footage in mind and imagine how the flow is marching in a spiral pattern. This explains why the heat transfer is augmented as the scale pitch ratio  $P_t/P_1$  increases.

## 5 Conclusions

In the present paper, six new types of elliptic scale-roughened surfaces are proposed and compared with the circular scale case. Sixteen types of scale-roughened models in total, including the



circular scale case with different scale heights, were simulated. The effects of scale pitch ratio, scale height, and Reynolds number on the heat transfer and flow characteristics are investigated. The reason why the scale-shaped roughness can considerably augment the heat transfer performance is presented by analyzing the flow behavior through the channels. Based on the results of the present study, the following conclusions can be drawn.

- (1) The pitch ratio, depth, and orientation of scales affect the flow and heat transfer characteristics of the channels significantly.
- (2) Generally, the elliptic scales with  $P_t > P_l$  enhance the heat transfer performance, while the elongated scales with  $P_t < P_l$  have lower Nusselt numbers and pressure drops compared with the circular scale-roughened channels.
- (3) The range of scale pitch ratio that has a prominent effect on the heat transfer augmentation and pressure drop is  $0.5 \leq P_t/P_l \leq 2$ .
- (4) Both the Nusselt number and pressure drop penalty are enhanced as the scale depth increases.
- (5) Flow through the scale-roughened channels is strongly rotated in the spanwise direction by the scale-shaped roughness. Bulk flow mixing is enhanced by the spirally marching flow.
- (6) Nusselt number ratios between the squeezed scale-roughened and smooth channel flows ( $Nu/Nu_\infty$ ) could be enhanced to around 6.5, which is a 40% improvement compared with the circular scale-roughened channels.

Considering the large number of parameters and consequent numbers of trials needed, a full optimization was not done in this work due to the computational expense. Our final goal is to apply this heat transfer enhancement technique to heat sinks and optimize them using VAT [24,27]. Therefore, the future work would be modeling heat sinks with elliptic scale-roughened surfaces based on VAT and obtaining closure either by experiment [26,28] and/or CFD code [19,29,30]. Besides, some experimental study will be carried out for the elliptic and circular scale-roughened surfaces considering there are something unclear about the data reported by Chang et al. [14]. Finally, with the help of a statistical tool for design of experiments or genetic algorithm, an elliptic scale-roughened heat sink could be designed and optimized in an hour, instead of days of CFD or experimental work.

## Acknowledgment

The support of a DARPA grant within the MACE program is gratefully acknowledged. The views, opinions, and/or findings contained in this article are those of the authors and should not be interpreted as representing the official views or policies, either expressed or implied, of the Defense Advanced Research Projects Agency or the Department of Defense.

## Nomenclature

$A_w$  = wetted surface  
 $c_p$  = specific heat  
 $D_h$  = hydraulic diameter  
 $e$  = scale height  
 $F_1, F_2$  = blending function  
 $f_{D_h}$  = fanning friction factor  
 $F_p$  = fin pitch  
 $H$  = channel height  
 $k$  = turbulence kinetic energy per unit mass  
 $k_f$  = thermal conductivity of the fluid.  $k_f = 0.0263 \text{ W/(m K)}$   
 $k_t$  = turbulent heat conductivity  
 $L$  = length of the channel  
 $\dot{m}$  = mass flow rate  
 $\langle m \rangle$  = porosity  
 $Nu_{D_h}$  = Nusselt number  
 $P_k$  = shear production of turbulence

$Pr$  = Prandtl number  
 $Pr_t$  = turbulent Prandtl number  
 $P_l$  = longitudinal scale pitch  
 $P_t$  = transverse scale pitch  
 $P_p$  = pumping power  
 $p$  = pressure  
 $q$  = heat flux  
 $Re$  = Reynolds number  
 $S$  = an invariant measure of the strain rate  
 $S_w$  = specific surface  
 $T_s$  = solid temperature  
 $T_f$  = fluid temperature  
 $\Delta T$  = difference between wall temperature and mean fluid temperature  
 $u$  = velocity  
 $x_i$  = components of the position vector  
 $X$  = first Cartesian coordinate  
 $y$  = the distance to the nearest wall  
 $Y$  = second Cartesian coordinate  
 $Z$  = third Cartesian coordinate

## Greek Symbols

$\alpha$  = turbulence model constant or scale attack angle  
 $\beta, \beta^*$  = turbulence model constant  
 $\varphi_1$  = represent any constant in the original  $k-\omega$  model ( $\sigma_k 1, \dots$ )  
 $\varphi_2$  = represent any constant in the transformed  $k-\varepsilon$  model ( $\sigma_k 2, \dots$ )  
 $\varphi$  = represent the corresponding constant in the SST model ( $\sigma_k, \dots$ )  
 $\eta_{\text{eff}}$  = effectiveness factor  
 $\mu$  = viscosity  
 $\nu$  = kinematic viscosity  
 $\rho$  = density  
 $\sigma_\varepsilon$  =  $k-\varepsilon$  turbulence model constant  
 $\sigma_k$  = turbulence model constant for the  $k$  equation  
 $\sigma_\omega$  =  $k-\omega$  turbulence model constant  
 $\omega$  = specific turbulence dissipation rate  
 $\Omega$  = volume

## Subscripts and Superscripts

$E$  = heat transfer enhanced channels  
 $\sim$  = an averaged values  
 $f$  = fluid phase  
 $s$  = solid phase  
 $t$  = turbulent  
 $\infty$  = comparative reference values

## Reference

- [1] Ligrani, P. M., Oliveira, M. M., and Blaskovich, T., 2003, "Comparison of Heat Transfer Augmentation Techniques," *AIAA J.*, **41**(3), pp. 337–362.
- [2] Taslim, M. E., Li, T., and Kercher, D. M., 1996, "Experimental Heat Transfer and Friction in Channels Roughened With Angled, V-Shaped, and Discrete Ribs on Two Opposite Walls," *Trans. ASME J. Turbomach.*, **118**(1), pp. 20–28.
- [3] Han, J. C., Zhang, Y. M., and Lee, C. P., 1991, "Augmented Heat Transfer in Square Channels With Parallel, Crossed, and V-Shaped Angled Ribs," *ASME J. Heat Transfer*, **113**(3), pp. 590–596.
- [4] Gao, X., and Sunden, B., 2001, "Heat Transfer and Pressure Drop Measurements in Rib-Roughened Rectangular Ducts," *Exp. Therm. Fluid Sci.*, **24**(1–2), pp. 25–34.
- [5] Park, J. S., Han, J. C., Huang, Y., Ou, S., and Boyle, R. J., 1992, "Heat Transfer Performance Comparisons of Five Different Rectangular Channels With Parallel Angled Ribs," *Int. J. Heat Mass Transfer*, **35**(11), pp. 2891–2903.
- [6] Cho, H. H., Wu, S. J., and Kwon, H. J., 2000, "Local Heat/Mass Transfer Measurements in a Rectangular Duct With Discrete Ribs," *ASME J. Turbomach.*, **122**(3), pp. 579–586.
- [7] Park, K., Choi, D.-H., and Lee, K.-S., 2004, "Optimum Design of Plate Heat Exchanger With Staggered Pin Arrays," *Numer. Heat Transfer, Part A*, **45**(4), pp. 347–361.

- [8] Khan, W. A., Culham, J. R., and Yovanovich, M. M., 2006, "The Role of Fin Geometry in Heat Sink Performance," *ASME J. Electron. Packag.*, **128**(4), pp. 324–330.
- [9] Zhou, F., and Catton, I., 2011, "Numerical Evaluation of Flow and Heat Transfer in Plate-Pin Fin Heat Sinks With Various Pin Cross-Sections," *Numer. Heat Transfer, Part A*, **60**(2), pp. 107–128.
- [10] Mahmood, G. I., Hill, M. L., Nelson, D. L., Ligrani, P. M., Moon, H. K., and Glezer, B., 2001, "Local Heat Transfer and Flow Structure on and Above a Dimpled Surface in a Channel," *ASME J. Turbomach.*, **123**(1), pp. 115–123.
- [11] Mahmood, G. I., and Ligrani, P. M., 2002, "Heat Transfer in a Dimpled Channel: Combined Influences of Aspect Ratio, Temperature Ratio, Reynolds Number, and Flow Structure," *Int. J. Heat Mass Transfer*, **45**(10), pp. 2011–2020.
- [12] Burgess, N. K., and Ligrani, P. M., 2005, "Effects of Dimple Depth on Channel Nusselt Numbers and Friction Factors," *ASME J. Heat Transfer*, **127**(8), pp. 839–847.
- [13] Mahmood, G. I., Sabbagh, M. Z., and Ligrani, P. M., 2001, "Heat Transfer in a Channel With Dimples and Protrusions on Opposite Walls," *J. Thermophys. Heat Transfer*, **15**(3), pp. 275–283.
- [14] Chang, S. W., Liou, T.-M., and Lu, M. H., 2005, "Heat Transfer of Rectangular Narrow Channel With Two Opposite Scale-Roughened Walls," *Int. J. Heat Mass Transfer*, **48**(19–20), pp. 3921–3931.
- [15] Chang, S. W., Liou, T. M., Chiang, K. F., and Hong, G. F., 2008, "Heat Transfer and Pressure Drop in Rectangular Channel With Compound Roughness of V-Shaped Ribs and Deepened Scales," *Int. J. Heat Mass Transfer*, **51**(3–4), pp. 457–468.
- [16] Chang, S. W., Yang, T. L., Liou, T.-M., and Fang, H. G., 2009, "Heat Transfer in Rotating Scale-Roughened Trapezoidal Duct at High Rotation Numbers," *Appl. Therm. Eng.*, **29**(8–9), pp. 1682–1693.
- [17] Chang, S. W., Yang, T. L., Liou, T.-M., and Hong, G. F., 2009, "Heat Transfer of Rotating Rectangular Duct With Compound Scaled Roughness and V-Ribs at High Rotation Numbers," *Int. J. Therm. Sci.*, **48**(1), pp. 174–187.
- [18] Chang, S. W., and Lees, A. W., 2010, "Endwall Heat Transfer and Pressure Drop in Scale-Roughened Pin-Fin Channels," *Int. J. Therm. Sci.*, **49**(4), pp. 702–713.
- [19] Zhou, F., DeMoulin, G. W., Geb, D. J., and Catton, I., 2012, "Closure for a Plane Fin Heat Sink With Scale-Roughened Surfaces for Volume Averaging Theory (VAT) Based Modeling," *Int. J. Heat Mass Transfer*, **55**(25–26), pp. 7677–7685.
- [20] Bardina, J. E., Huang, P. G., and Coakley, T. J., 1997, "Turbulence Modeling Validation, Testing, and Development," NASA Technical Memorandum.
- [21] Menter, F. R., 1994, "Two-Equation Eddy-Viscosity Turbulence Models for Engineering Applications," *AIAA J.*, **32**(8), pp. 1598–1605.
- [22] Menter, F. R., Kuntz, M., and Langtry, R., 2003, "Ten Years of Industrial Experience With the SST Turbulence Model," *Turbul. Heat Mass Transfer*, **4**, pp. 625–632.
- [23] Wee, H., Zhang, Q., Ligrani, P. M., and Narasimhan, S., 2008, "Numerical Predictions of Heat Transfer and Flow Characteristics of Heat Sinks With Ribbed and Dimpled Surfaces in Laminar Flow," *Numer. Heat Transfer, Part A*, **53**(11), pp. 1156–1175.
- [24] Travkin, V. S., and Catton, I., 2001, "Transport Phenomena in Heterogeneous Media Based on Volume Averaging Theory," *Adv. Heat Transfer*, **34**, pp. 1–144.
- [25] Whitaker, S., 1972, "Forced Convection Heat Transfer Correlations for Flow in Pipes, Past Flat Plates, Single Cylinders, Single Spheres, and for Flow in Packed Beds and Tube Bundles," *AIChE J.*, **18**(2), pp. 361–371.
- [26] Zhou, F., Hansen, N. E., Geb, D. J., and Catton, I., 2011, "Obtaining Closure for Fin-and-Tube Heat Exchanger Modeling Based on Volume Averaging Theory (VAT)," *ASME J. Heat Transfer*, **133**(11), p. 111802.
- [27] Catton, I., 2011, "Conjugate Heat Transfer Within a Heterogeneous Hierarchical Structure," *ASME J. Heat Transfer*, **133**(10), p. 103001.
- [28] Geb, D., Zhou, F., and Catton, I., 2012, "Internal Heat Transfer Coefficient Determination in a Packed Bed From the Transient Response Due to Solid Phase Induction Heating," *ASME J. Heat Transfer*, **134**(4), p. 042604.
- [29] Zhou, F., Hansen, N. E., Geb, D. J., and Catton, I., 2011, "Determination of the Number of Tube Rows to Obtain Closure for Volume Averaging Theory Based Model of Fin-and-Tube Heat Exchangers," *ASME J. Heat Transfer*, **133**(12), p. 121801.
- [30] Zhou, F., and Catton, I., 2012, "Volume Averaging Theory (VAT) Based Modeling and Closure Evaluation for Fin-and-Tube Heat Exchangers," *Heat Mass Transfer*, **48**(10), pp. 1813–1823.